RSC Advances

PAPER

View Article Online
View Journal | View Issue

Cite this: *RSC Adv.*, 2025, **15**, 33946

A zero-dimensional $(C_6H_9N_2)_3[BiCl_6]$ hybrid material: synthesis and structural, optical, and electrical conductivity

Rima Altalib, [a] Arafet Ghoudi, [a] Mohamed Tliha,[b] Raja Naouari,[c] Walid Rekik,[d] Jerome Lhoste [e] and Abderrazek Oueslati *[a]

Received 11th March 2025
Accepted 8th September 2025

DOI: 10.1039/d5ra01766a

rsc.li/rsc-advances

The organic–inorganic hybrid compounds have attracted considerable attention due to their exceptional properties and diverse applications. This study successfully synthesized the hybrid compound $(C_6H_9N_2)_3[BiCl_6]$ *via* a slow evaporation technique at room temperature. Structural analysis confirmed a triclinic crystal system within the $P\bar{1}$ space group, while thermal investigations revealed a phase transition at 420 K. Optical characterization through UV-visible absorption spectroscopy highlighted its semiconducting nature. Electrical and dielectric measurements performed using complex impedance spectroscopy (CIS) demonstrated a strong dependence on both frequency and temperature. Nyquist plots (*-Z″ vs. Z′*) exhibited a single semicircular arc, indicative of non-Debye relaxation behavior. The AC conductivity exhibits behavior consistent with Jonscher's universal power law, while temperature-dependent analysis indicates that the correlated barrier-hopping (CBH) model governs the predominant conduction mechanism. Notably, the material exhibits a high dielectric constant, underscoring its potential for energy storage applications.

1 Introduction

Organic–inorganic hybrid halide compounds have attracted widespread scientific interest worldwide, owing to their distinctive and intriguing physicochemical properties,[1–5] opening doors to groundbreaking research and diverse industrial applications. These materials hold immense promise in fields like optoelectronics,[6,7] solid electrolytes,[8] photovoltaics,[9] nonlinear optics,[10,11] energy storage,[12,13] biomedicine,[11,14] and various other domains. As researchers strive to meet the demands for low-cost and highly functional materials with adaptable properties, organic–inorganic hybrid compounds are emerging as a key area of focus.

These hybrid systems, which combine organic spacer cations (such as aliphatic, cyclic, aromatic, and heteroatomic cations) with inorganic components, offer an exciting platform for innovation.[15–17] The intricate structure of these materials, comprising molecular-scale composites, allows for the integration of properties from both organic and inorganic elements, resulting in novel substances with distinctive characteristics.[18] This versatility makes organic–inorganic hybrids highly attractive for electronic devices due to their low exciton binding energy, reduced trap density, and favorable electrical and dielectric characteristics, including high permittivity, excellent conductivity, and low dielectric loss.

Among the diverse range of organic–inorganic hybrids, a particularly intriguing subclass includes compounds that combine amines with bismuth and halogens. Halogeno-bismuthates(III) with organic cations have attracted considerable attention for their potential to exhibit ferroelectric properties and proton conductivity.[19–23]

As part of our current study, we report our investigations on a new bismuth-based organic–inorganic compound with a general chemical formula of $(C_6H_9N_2)_3[BiCl_6]$ which presents a unique combination of bismuth halide chemistry and organic molecular components. Unlike many conventional materials, this compound integrates the favorable electrical and dielectric characteristics of both organic and inorganic segments, resulting in enhanced performance suitable for energy storage applications. Our findings show that the high dielectric constant at low frequencies, coupled with significant AC conductivity and frequency-dependent behavior, positions $(C_6H_9N_2)_3[BiCl_6]$ as a promising candidate for versatile electronic applications.

[a]*Laboratory of Spectroscopic Characterization and Optical Materials, Faculty of Sciences, University of Sfax, B.P. 1171, 3000 Sfax, Tunisia. E-mail: oueslatiabderrazek@yahoo.fr*

[b]*Department of Physics, Al-Qunfudah University College, Umm Al-Qura University, Saudi Arabia*

[c]*Physics Department, Faculty of Science, Al Baha University, 65779-7738 Al Aqiq, Saudi Arabia*

[d]*Laboratory Physical-Chemistry of Solid State, Chemistry Department, Faculty of Sciences of Sfax, University of Sfax, BP 1171, Sfax, 3000, Tunisia*

[e]*Institut des Molécules et Matériaux Du Mans (IMMM)– UMR-6283 CNRS, Le Mans Université, Avenue Olivier Messiaen, F-72085 Le Mans Cedex 9, France*

2 Experimental details

2.1 Chemical preparation of $(C_6H_9N_2)_3[BiCl_6]$

The organic–inorganic compound $(C_6H_9N_2)_3[BiCl_6]$ was prepared through a solvent evaporation technique, following an approach comparable to those used in the synthesis of other hybrid materials previously documented.[24–26] This method represents a significant advancement in the field as it enables crystallization to occur under milder conditions, specifically at room temperature, in contrast to traditional methods, which often require high temperatures or prolonged reaction times. The use of this method not only facilitates the orderly arrangement of the constituent molecules but also promotes the growth of well-defined crystalline structures.

The selection of bismuth and halogen as key components in our hybrid material was guided by their known roles in enhancing electronic properties. Bismuth, in particular, has been extensively studied for its favorable optoelectronic characteristics, while halogens are critical in stabilizing the structure at a molecular level. These components not only contribute to the material's thermal stability but also facilitate charge transport, which is essential for its application in semiconductors and energy storage systems.

To synthesize crystals of $(C_6H_9N_2)_3[BiCl_6]$, dissolve 0.1 g (0.925 mmol) of 2-amino-5-picoline ($C_6H_8N_2$), 0.0972 g (0.308 mmol) of bismuth(III) chloride ($BiCl_3$), and 0.75 mL of 36.5% hydrochloric acid (12 M, corresponding to 9.24 mmol HCl) of hydrochloric acid (HCl) in a small quantity of distilled water. Allow the solution to stand at room temperature (around 28 °C). As the solvent slowly evaporated, millimetre-sized yellow crystals formed (Fig. 1), which were filtered and air-dried.

2.2 Single-crystal diffraction data collection and structure determination

A high-quality single crystal of the investigated compound (0.23 × 0.19 × 0.13 mm^3) was meticulously selected using a polarizing microscope, glued, and mounted at 296 K on a four-circle BRUKER APEX II area-detector diffractometer for structural analysis. Reflection data were collected using molybdenum Kα radiation ($\lambda = 0.71073$ Å) monochromated by a graphite filter.

Fig. 1 Crystals of the $(C_6H_9N_2)_3[BiCl_6]$ compound.

Intensity measurements were systematically captured through the APEX 2 software platform.[27] Empirical absorption corrections of multi-scan methodology were implemented using the SADABS program.[27] Crystal structure determination was performed within the centrosymmetric $P\bar{1}$ space group, employing direct methods *via* the SHELXS-2014 program[28] integrated into the WINGX interface.[29] Non-hydrogen atomic components underwent anisotropic refinement. All hydrogen atoms were positioned geometrically using the HFIX command in SHELXL-2014[28] and refined isotropically following a riding model, with U_{iso}(H) set to −1.200 U_{eq}(C) and −1.200 U_{eq}(N). The N–H and C–H bond lengths were constrained to 0.86 Å and 0.93 (or 0.96 Å), respectively. The concluding structural refinement yielded excellent reliability factors: $R_1 = 0.035$ and $wR_2 = 0.087$. Crystallographic visualizations were generated using Diamond3.2 software. A detailed summary of crystallographic data, least-squares refinement parameters, atomic coordinates, isotropic temperature factors, bond lengths, bond angles, and hydrogen bonding interactions is provided in Table 1 and S1–S3.

The supplementary crystallographic information for the referenced compound is archived under the identifier CCDC 2366479. This comprehensive dataset is freely accessible to researchers and interested parties *via* the Cambridge Crystallographic Data Center's online repository at **www.ccdc.cam.ac.uk/data_request/cif**.

Table 1 Crystallographic data and structure refinements of $(C_6H_9N_2)_3[BiCl_6]$

Formula	$(C_6H_9N_2)_3[BiCl_6]$
Color/Shape	Yellow/Prism
Formula weight ($gmol^{-1}$)	749.13
Crystal system	Triclinic
Space group	$P\bar{1}$
Density	1.845
Crystal size (mm)	0.23 × 0.19 × 0.13
Temperature (K)	296(2)
Diffractometer	Bruker APEXII
a (Å)	14.3578(3)
b (Å)	14.4070(3)
c (Å)	14.4113(3)
α (°)	104.5580(10)
β (°)	104.4070(10)
γ (°)	100.5740(10)
V ($Å^3$)	2696.60(10)
Z	4
Radiation type	Mo Kα (0.71073 Å)
Absorption correction	Multi-scan
θ range for data collection(°)	$1.518 \leq \theta \leq 27.497$
Measured reflections	27 100
Independent reflections	11 839
Observed data [I > 2σ (I)]	7733
Index ranges	$h = -18 \rightarrow 18$
	$k = -16 \rightarrow 18$
	$l = -18 \rightarrow 18$
F(000)	1448
Number of parameters	559
R_1	0.035
wR_2	0.087
Goof	1.017

2.3 Instrumentation and methodologies for morphological, IR, thermal, optical, and electrical characterizations

The compound's elemental composition and chemical properties were examined using Energy-Dispersive X-ray Spectroscopy (EDX) with a Bruker Quantax 100 Easy EDX detector.

The solid-state infrared spectrum of $(C_6H_9N_2)_3[BiCl_6]$ was obtained using a Nicolet NXR FTIR spectrometer, at room temperature.

The DSC measurements were completed by a PerkinElmer DSC-7 instrument, employing a heating rate of 5 K min^{-1}. The temperature cycle, spanning from 300 K to 480 K, was designed to determine the temperatures of phase transitions.

Ultraviolet-visible (UV-vis) spectra of the powdered sample were acquired using a Jobin Yvon Fluoromax-4 spectrofluorometer alongside a Shimadzu UV-3101PC spectrophotometer, operating in both absorbance and reflectance modes, with a slit width of 20 nm and a LISR-3100 integrated sphere; $BaSO_4$ served as the reference material.

For the impedance study, the powder obtained from grinding the crystals was compacted into a pellet (8 mm in diameter and 1.1 mm in thickness). Thin silver films, approximately a few nanometers in thickness, were then manually deposited on both flat faces of the pellet. The silver-coated pellet was positioned in the Linkam LTS420 temperature control system. Complex impedance spectra were recorded over a temperature range of 333–443 K and a broad frequency range of 10 Hz to 5 MHz using a Solartron 1260 analyzer.

3 Results and discussion

3.1 Insight into the crystal structure

In a previous study, we reported the chemical synthesis and characterization of $(C_6H_9N_2)_2[Sb_2Cl_8]$, a compound that crystallizes in the triclinic system at room temperature, adopting the centrosymmetric space group $P\bar{1}$. The lattice parameters for this compound were determined as follows: $a = 7.9767(7)$ Å, $b = 9.0843(8)$ Å, $c = 9.3456(8)$ Å, $\alpha = 86.352(6)$ °, $\beta = 69.069(5)$ °, $\gamma = 74.829(5)$ ° and $V = 610.14(10)$ Å^3.[30] In this work, the substitution of antimony by bismuth results in several structural modifications. As detailed in Table 1, the new hybrid material $(C_6H_9N_2)_3[BiCl_6]$ also adopts triclinic symmetry, crystallizing at 296(2) K in the centrosymmetric space group $P\bar{1}$. The unit cell parameters for this compound are as follows: $a = 14.3578(3)$ Å; $b = 14.4070(3)$ Å; $c = 14.4113(3)$ Å; $\alpha = 104.5580(10)$ °; $\beta = 104.4070(10)$ °; $\gamma = 100.5740(10)$ °; $V = 2696.60(10)$ Å^3 and $Z = 4$. The crystal structure of this supramolecular compound comprises $[BiCl_6]^{3-}$ anions and protonated amine $(C_6H_9N_2)^+$ cations, which are interconnected through N–H···Cl hydrogen bonds and weaker C–H···Cl interactions (Fig. 2).

The asymmetric unit of $(C_6H_9N_2)_3[BiCl_6]$, depicted in Fig. 3, consists of two crystallographically independent bismuth(III) cations, each coordinated by six chloride ions, forming $[BiCl_6]^{3-}$ anions, along with six organic cations $(C_6H_9N_2)^+$. It is noteworthy that all atoms in the asymmetric unit are in general positions (Wyckoff site 2i).

As shown in Fig. S1, the $[BiCl_6]^{3-}$ anions are arranged in stacks along the[1–10] direction, creating inorganic pseudo-layers. The octahedral $[BiCl_6]^{3-}$ units are spaced apart with a minimum Bi–Bi distance of 8.8060(4) Å. Within the $[BiCl_6]^{3-}$ anions, the Bi–Cl bond lengths vary from 2.6140(14) to 2.8061(15) Å for $Bi1Cl_6$, and from 2.5961(14) to 2.8274(14) Å for Bi_2Cl_6. The *cis*-Cl–Bi–Cl bond angles span from 86.15(5) ° to 94.85(5) ° for $Bi1Cl_6$, and from 87.11(5) ° to 93.31(4) ° for Bi_2Cl_6 (Table S2). These geometric features are consistent with those observed in other compounds containing $BiCl_6$ octahedra.[31–34] Based on the

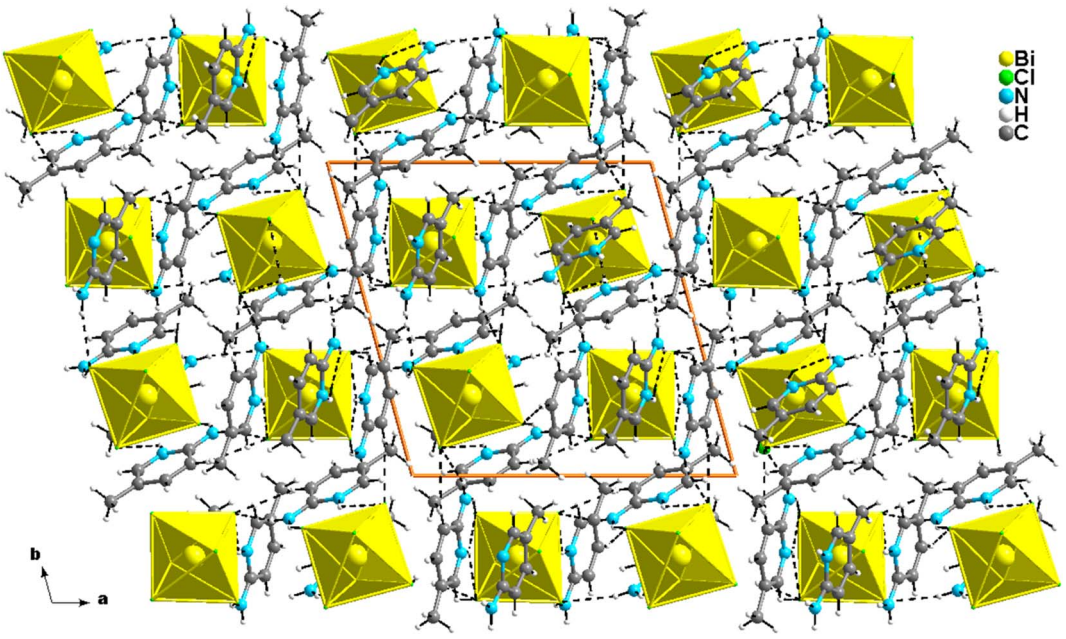

Fig. 2 Projection of the structure of $(C_6H_9N_2)_3[BiCl_6]$ along the crystallographic *c*-axis.

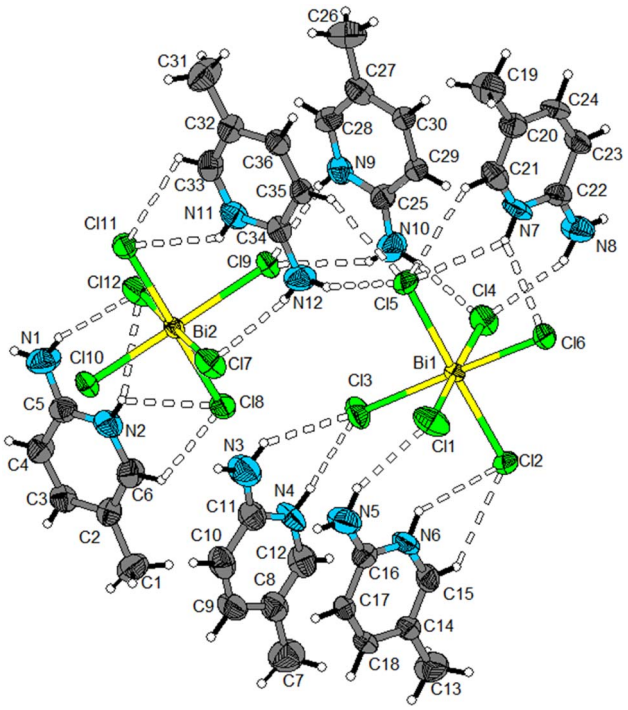

Fig. 3 The asymmetric unit of $(C_6H_9N_2)_3[BiCl_6]$. Displacement ellipsoids are drawn at the 50% probability level. Dashed lines represent hydrogen bonds.

geometrical parameters of the $[BiCl_6]^{3-}$ anions in our compound, the distortion indices (DI) were calculated using the method outlined in ref. 35.

$$\mathrm{DI(Bi-Cl)} = \sum_{i=1}^{n_1} \frac{|d_i - d_m|}{n_1\ d_m} \quad (1)$$

$$\mathrm{DI(Cl-Bi-Cl)} = \sum_{i=1}^{n_2} \frac{|a_i - a_m|}{n_2\ a_m} \quad (2)$$

where d is the Bi–Cl distance, a refers to the Cl–Bi–Cl angle, m refers to the average value, while $n_1 = 6$ and $n_2 = 12$ for octahedral environment.

The distortion indices obtained for the $[BiCl_6]^{3-}$ anions, DI (Bi1–Cl) = 0.0224, DI (Bi_2–Cl) = 0.0233, and DI (Cl–Bi–Cl) = 0.022 and 0.020 for $Bi1Cl_6$ and Bi_2Cl_6, respectively, indicate that the bismuth coordination geometry is a slightly distorted octahedron. This distortion arises from intermolecular hydrogen bonds between the organic cations and the $[BiCl_6]^{3-}$ octahedra. The negative charge on the hexachlorobismuthate(III) anions $[BiCl_6]^{3-}$ is balanced by the protonated amines $(C_6H_9N_2)^+$, which are arranged in layers parallel to the inorganic layers, as seen in Fig. 4. The structural of the $(C_6H_9N_2)_3[BiCl_6]$ is composed of alternating organic and inorganic layers. The geometric characteristics of the protonated amines, detailed in Table S3, align with those observed in the antimony-based compound.[30,36] The interaction between the organic cations and the hexachlorobismuthate(III) anions is facilitated by medium N–H···Cl hydrogen bonds and weak C–H···Cl interactions. As illustrated in Fig. 2 and 3, each $(C_6H_9N_2)^+$

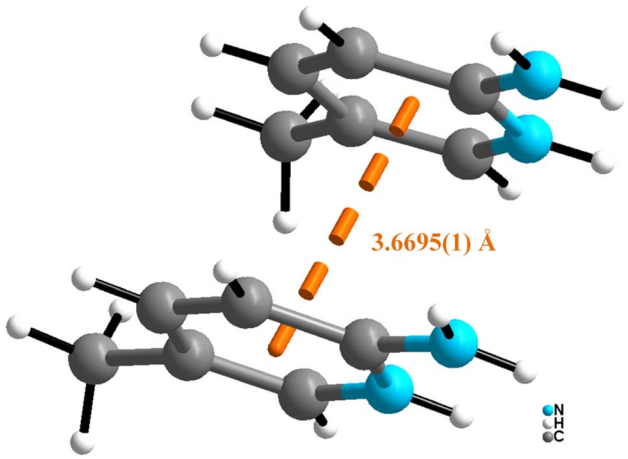

Fig. 4 π ···π interactions in the structure of $(C_6H_9N_2)_3[BiCl_6]$.

cation forms N–H···Cl and C–H···Cl bonds with several $[BiCl_6]^{3-}$ anions. The N···Cl distances within the hydrogen bonds range from 3.164(5) to 3.617(5) Å, while the C···Cl distances vary between 3.463(7) and 3.629(6) Å. The N–H···Cl and C–H···Cl bond angles range from 122.8° to 170.0° and from 118.8° to 147.6°, respectively (Table S4). Additionally, the $(C_6H_9N_2)^+$ organic cations engage in π···π interactions with one another. These interactions occur in a parallel-displaced configuration between the amine aromatic rings.[37,38] Within the π···π interactions in $(C_6H_9N_2)_3[BiCl_6]$, the centroid-to-centroid distance between two parallel planes of aromatic rings from adjacent protonated amines is 3.6659(1) Å (Fig. 4), the interring dihedral $\alpha = 1.808°$, the slip angle $\beta = 10.659°$, and the perpendicular distance of CgI from ring CgJ is equal to 3.4572 Å. Notably, the π···π interactions in $(C_6H_9N_2)_3[BiCl_6]$ are slightly weaker than those observed in the chlorine-based compound $(C_6H_9N_2)_2[Sb_2Cl_8]$, where the shortest centroid-to-centroid distance between two aromatic rings is 3.6473(2) Å.[30]

3.2 EDX results

Fig. 5 presents the EDX spectrum of the synthesized compound. Distinct characteristic X-ray peaks corresponding to C, Bi, N, and Cl are identified and labeled in the spectrum. The quantified weight percentages were found to be 32.45% carbon, 32.33% bismuth, 12.54% nitrogen, and 22.68% chlorine. In addition, minor peaks of Au are also visible in the spectrum; these originate from the thin gold coating deposited on the sample surface during EDX preparation to improve conductivity and reduce charging effects, and therefore do not belong to the intrinsic composition of the compound.

3.3 Vibrational properties

Fig. 6 presents the infrared (IR) spectrum of the $(C_6H_9N_2)_3[BiCl_6]$ compound. The FT-IR analysis of this hybrid material highlights the presence of characteristic vibrational modes originating from the organic cation.[39–42] A broad absorption band observed between 3200 and 3400 cm^{-1} is attributed to the N–H stretching vibrations of the amino groups, while weaker

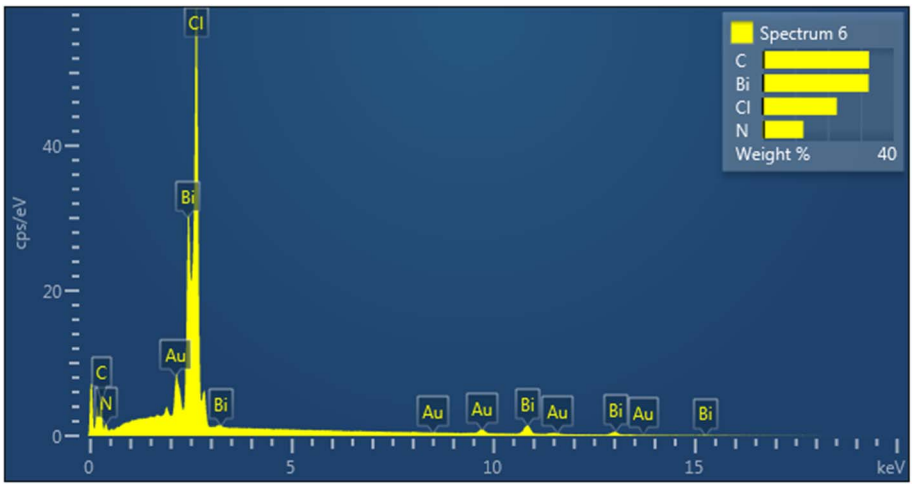

Fig. 5 EDX analysis of $(C_6H_9N_2)_3[BiCl_6]$.

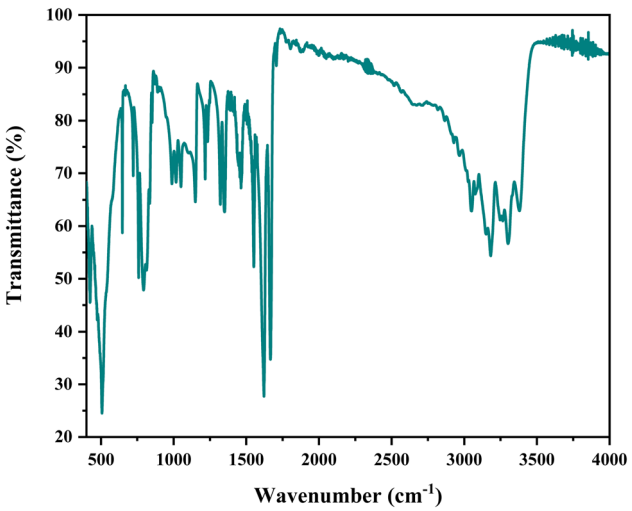

Fig. 6 Infrared spectrum of $(C_6H_9N_2)_3[BiCl_6]$.

peaks in the 2850–3100 cm^{-1} range correspond to C–H stretching vibrations. The intense band appearing between 1600 and 1650 cm^{-1} is assigned to the overlapping contributions of C=C stretching in the aromatic ring and N–H bending vibrations. In the 1500–1300 cm^{-1} region, the observed features are associated with C–N stretching and C–H bending modes. Furthermore, absorptions detected around 1000–1100 cm^{-1} and 700–900 cm^{-1} correspond to in-plane and out-of-plane C–H bending vibrations of the pyridine ring, respectively, confirming the integrity of the organic framework within the hybrid structure.

3.4 Thermal stability studies

Differential Scanning Calorimetry (DSC) is a powerful technique for analyzing phase transitions, including melting, glass transitions, and exothermic decompositions, which are relevant to various applications in fields such as optoelectronics and photovoltaics. DSC is highly sensitive to energy or heat capacity changes associated with these transitions. To investigate the phase transition of hybrid metal halides induced by external thermal stimulation, DSC measurements were conducted over a temperature range from ambient temperature to 480 K, as illustrated in Fig. 7. The DSC results revealed two anomalous thermal peaks at approximately 420 K and 452 K during the heating process, consistent with similar compounds.[43,44] The peak at $T_1 = 420$ K corresponds to the material's phase transition temperature. The second endothermic peak, located at around $T_2 = 452$ K, corresponds to the melting of the sample. The enthalpy change (ΔH) of the phase transition was calculated by integrating the DSC curve's peak area, yielding an estimated value of 28.535 J mol^{-1}. The obtained entropy of the phase transition is equal to 0.0679 J mol^{-1} K^{-1}.

The nature of the phase transition can be determined using the Boltzmann formula:[45]

$$\Delta S = R \ln \Omega = R \ln \frac{N1}{N2} \quad (3)$$

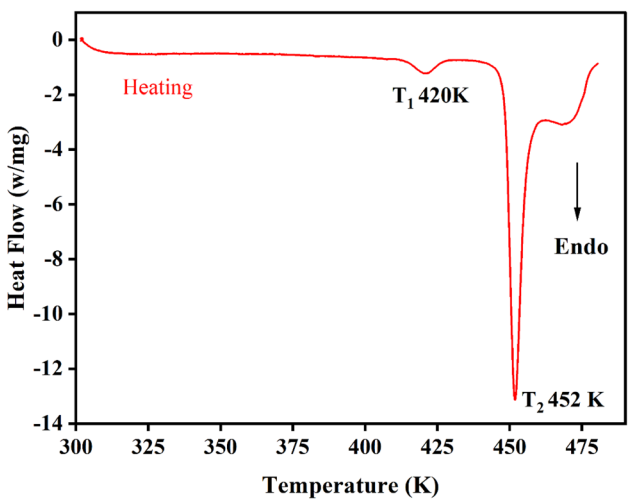

Fig. 7 DSC curves of $(C_6H_9N_2)_3[BiCl_6]$.

here, $N1$ and $N2$ represent the number of conformations at high and low temperatures, respectively, and $R = 8.31$ J mol^{-1} K^{-1} is the ideal gas constant. Since ΔS is smaller than R ln 2, the phase transition at T_1 is not purely of the order–disorder transition type.[46]

In comparison with other recently reported lead-free halide compounds, such as those described in *Chin. Chem. Lett.* 2023, 34, 107980, the phase transition temperature of $(C_6H_9N_2)_3[BiCl_6]$ at 420 K demonstrates promising thermal stability. While some similar hybrid halide materials exhibit phase transitions at lower temperatures, the relatively high transition temperature observed in our study suggests enhanced thermal robustness, which is beneficial for high-temperature applications in energy storage and optoelectronic devices. This thermal stability, combined with the material's other advantageous properties, positions $(C_6H_9N_2)_3[BiCl_6]$ as a competitive candidate among lead-free halide hybrids for practical technological applications.

3.5 Optical properties

3.5.1 UV-visible absorbance. Fig. 8 represents the UV-visible absorption spectrum of the synthesized compound $(C_6H_9N_2)_3[BiCl_6]$. The graph shows five absorption peaks at 214, 300, 327, 355, and 405 nm. These results are comparable to those of other MX_6 hybrid materials.[47,48] The pyridine rings undergo π–π* and n–π* transitions, which result in three UV bands at 213, 300, and 327 nm.[49] The band at 355 nm represents the absorption of electron–hole pairs inside the $[BiCl_6]^{3-}$ inorganic chains as they transition from the valence to conduction bands. Additionally, a weak absorption band at 405 nm arises due to charge transfer interactions between the organic ligand and the inorganic component.

3.5.2 Optical band gap. In the context of semiconductors or insulators, E_g denotes the minimal energy necessary to promote an electron from the valence band to the conduction band by photon absorption. The energy gap determines a material's optical characteristics, such as its absorption spectrum, color, and transparency. For these reasons, E_g is crucial in a variety of fields, including photovoltaics, photoluminescence, and laser technology.[50,51]

Marotti and Henríque and their co-workers[52,53] discovered that E_g can be calculated from the observed reflectance spectrum ($R(\lambda)$), which corresponds to the maximum of the $(1/R(\lambda))(dR(\lambda)/d\lambda)$ function. The insert of Fig. 8 shows a prominent peak at 370 nm, which, taking into account the relationship between energy and wavelength (E(eV) = 1239.8/λ(nm)), results in an E_g of 3.35 eV for $(C_6H_9N_2)_3[BiCl_6]$, which is similar to those of ZnO (3.34 eV)[54] and stays in the typical range of semiconductors (0.5 eV to 5 eV), particularly wide energy gap semiconductors.

To determine whether the optical band transition mode of the investigated materials is direct or indirect, we employed Tauc's law:

$$F_{KM}(R(\lambda))h\nu = B(h\nu - E_g)^n \quad (4)$$

where h refers to the Planck's constant (~6.6×10^{-34} J), $F_{KM}(R(\lambda))$ is the Kubelka–Munk function ($F_{KM}(R(\lambda)) = (1\ R(\lambda))^2/2R(\lambda)$), while the incident photon's energy is given by $h\nu$ (in eV), and B is the band edge sharpness constant. The exponent n reflects the nature of the optical transition: $n = 1/2$ for a permitted direct transition and $n = 2$ for an allowed indirect band gap.[55]

The Tauc plot is presented in Fig. 9. The E_g value was calculated by intersecting the extrapolation of the linear plot with the x-axis. Fig. 9 clearly shows that a satisfactory match is obtained for $n = 1/2$, resulting in a band gap value comparable to that obtained using the Marotti approach (3.35 eV). In conclusion, our analysis reveals that $(C_6H_9N_2)_3[BiCl_6]$ exhibits a direct transition with a band gap of 3.18 eV.

3.5.3 The Urbach energy E_u. Another key parameter that provides valuable information about our compound is the

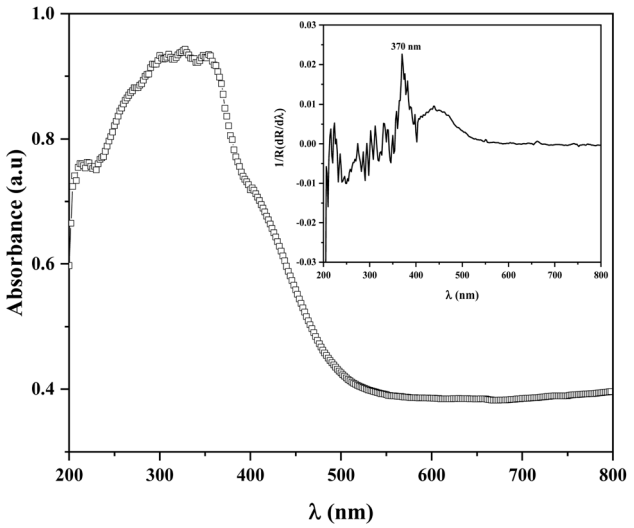

Fig. 8 UV-vis absorption spectrum of $(C_6H_9N_2)_3[BiCl_6]$. The inset represents the variation of $(1/R(\lambda))(dR(\lambda)/d\lambda)$ as a function of wavelength.

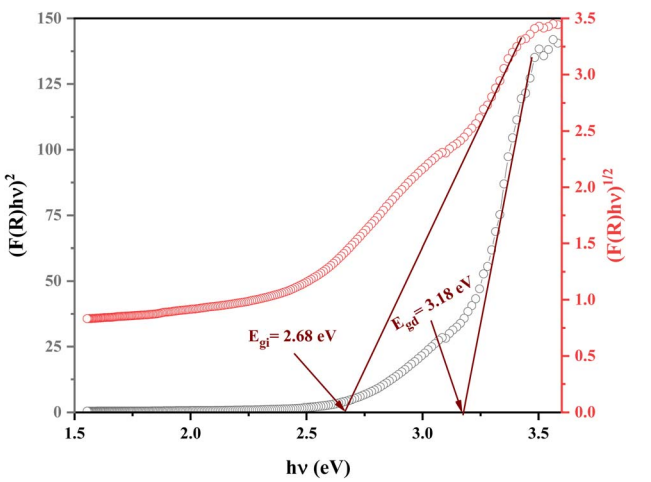

Fig. 9 Tauc plot for $(C_6H_9N_2)_3[BiCl_6]$.

Urbach energy (E_u). This parameter, commonly associated with amorphous and disordered materials, can be evaluated using the Urbach model.[56] E_u reflects the width of the exponential tail that represents localized states situated between the valence and conduction bands. Typically, the incorporation of a high concentration of foreign atoms into a crystal lattice increases structural disorder, which in turn leads to higher Urbach energy values and a consequent narrowing of the effective optical band gap. As highlighted by Yang *et al.*,[57] the Urbach tail originates from both phonon interactions and structural fluctuations. The Urbach energy can be extracted using the following relation,

$$\ln(\alpha) = \ln(B) + \frac{h\nu - E_g}{E_u} \quad (5)$$

where B is a constant: it is obtained directly from the slope of the linear region in the plot of $\ln(\alpha)$ *versus* photon energy ($h\nu$) (Fig. 10). For our compound, E_u is estimated at 0.47 eV, which indicates a pronounced degree of disorder. Indeed, materials with large E_u values are more prone to transform weak structural bonds into defects. According to Husain *et al.*,[58] such elevated Urbach energy values are typically associated with a high density of localized states.

3.5.4 The optical extinction. The optical behavior of the investigated sample is governed by the interaction between the material and the electric field of the incident electromagnetic radiation. Several physical parameters are influenced by the absorption of this radiation, including the sample thickness, photoconductivity, refractive index (n), and extinction coefficient (k). The attenuation of electromagnetic energy within the sample is strongly dependent on both the crystalline structure and the surface morphology of the illuminated material.

The propagation velocity of the electromagnetic wave through the compound, as a function of frequency (ν), can be expressed using the complex refractive index (N),[59]

$$N = n - iK \quad (6)$$

where n represents the real component associated with wave velocity, and K denotes the extinction coefficient, which characterizes the damping of the oscillation amplitude of the incident wave. Furthermore, k is directly related to the absorption coefficient (α), as reported in earlier works:[59]

$$K(\lambda) = \frac{\alpha(\lambda)\lambda}{4\pi} \quad (7)$$

Fig. S2 illustrates the variation of the extinction coefficient (K) with photon energy ($h\nu$). A noticeable decrease in K is observed as the photon energy increases. This reduction may be attributed to a decline in the incident photon energy near the material's surface under illumination, as well as to possible distortions within the crystal lattice.

3.5.5 Refractive index (n). The refractive index (n) is one of the essential optical parameters of a material, as it plays a central role in its interaction with light. It is particularly significant in defining the optical response and in the selection of materials for spectral dispersion applications. The variation of this parameter is therefore of great importance for numerous technological uses. The optical refractive index can be determined from reflectance spectra using a straightforward relation.[48]

$$n(\lambda) = \frac{1+R}{1-R} + \sqrt{\frac{4R}{(1-R)^2} - K(\lambda)} \quad (8)$$

Fig. 11 presents the dependence of the refractive index (n) on wavelength (λ) at room temperature. It can be observed that n attains relatively high values in the visible region.

Moreover, the spectral variation of n follows Cauchy's law, which can be expressed by the well-known empirical relationship.[60]

$$n(\lambda) = n_1 + \frac{n_2}{\lambda^2} + \frac{n_3}{\lambda^4} \quad (9)$$

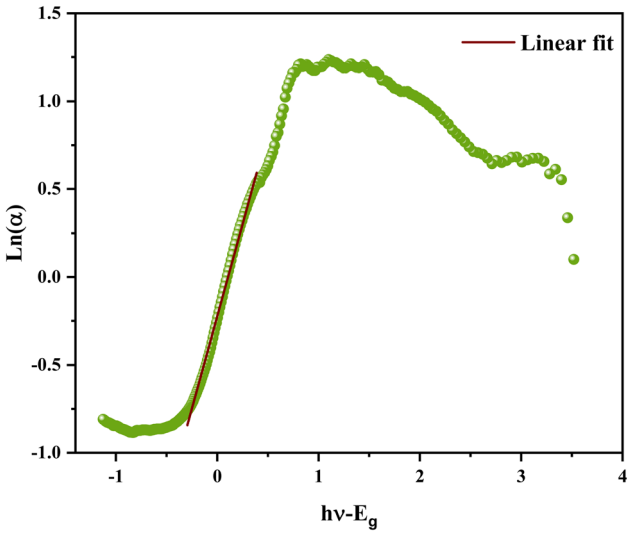

Fig. 10 $\ln(\alpha)$ *vs.* energy $h\nu$.

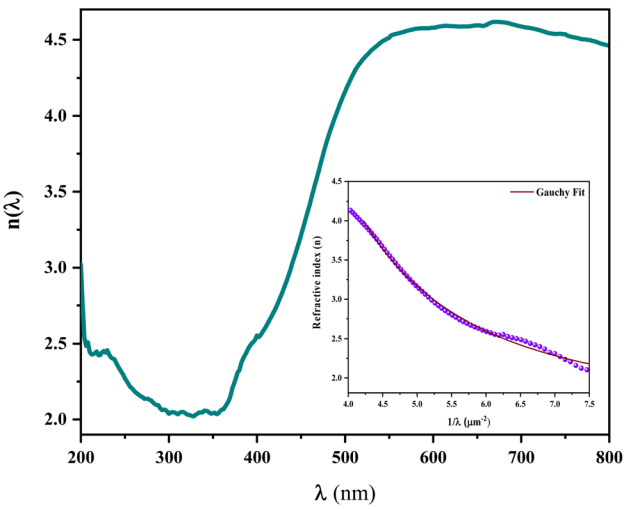

Fig. 11 Evolution of the refractive index n against wavelength λ (inset) fit of refractive index n using Cauchy's law.

By fitting our experimental data with this relation (inset of Fig. 11), the constants of Cauchy's law were extracted: $n_0 = 1.528$, $n_1 = 32.262\ \mu m^2$, and $n_2 = 199.828\ \mu m^4$.

3.5.6 Single-effective oscillator model: dispersion energy parameters. In 1973, Wemple and DiDomenico introduced a model that enables the analysis of several important optical parameters, including the dispersion energy (E_d), which reflects the oscillator strength of interband transitions, and the single-oscillator energy (E_0), corresponding to the average interband transition energy. This approach also provides insights into the dispersion of the refractive index through the single-effective oscillator model.[59,61] According to this model, the optical data can be described by the following expression:

$$n^2 - 1 = \frac{E_0 E_d}{E_0^2 - (h\nu)^2} \quad (10)$$

where $h\nu$ is the photon energy, n is the refractive index, E_0 is the single-oscillator energy, and E_d represents the dispersion energy, quantifying the average strength of inter-band optical transitions. These parameters are extracted from the slope and intercept of the linear plot of $(n^2\text{-}1)^{-1}$ *versus* $(h\nu)^2$, as shown in Fig. 12(a). From the fit, the slope corresponds to $1/E_0E_d$, while the intercept with the vertical axis yields $1/E_d$. Based on this analysis, the calculated values are $E_0 = 7.05$ eV and $E_d = 14.5$ eV.

Using the same framework, the oscillator strength (S_0) and the oscillator wavelength (λ_0) of the sample can be determined through the following relation. Fig. 12(b) shows the variation of $(n^2\text{-}1)^{-1}$ with λ^{-2}. A linear fitting of this curve provides the values $S_0 = 6 \times 10^{-5}\ nm^{-2}$ and $\lambda_0 = 188$ nm. Furthermore, the Wemple–DiDomenico model also enables the determination of the moments of the optical spectrum, M_{-1} and M_{-3}, which are related to the single-oscillator energy (E_0) and dispersion energy (E_d). The computed values of these moments are $M_{-1} \approx 2.05$ and $M_{-3} \approx 0.20\ eV^{-2}$.

3.5.7 Dielectric properties under optical energy. The real (ε_1) and imaginary (ε_2) components of the complex dielectric constant (ε^*) for the studied compound are directly related to the refractive index (n) and extinction coefficient (K). These values were calculated using the standard relations connecting ε^*, n, and K.[62]

$$\varepsilon^*(\lambda) = \varepsilon_1(\lambda) - i\varepsilon_2(\lambda) = (n(\lambda) - iK(\lambda))^2 \quad (11)$$

$$\varepsilon_1(\lambda) = n^2(\lambda) - K^2(\lambda) \quad (12)$$

$$\varepsilon_2(\lambda) = 2n(\lambda)K(\lambda) \quad (13)$$

Fig. 13 present the variation of the real part (ε_1, the dispersion curve) and the imaginary part (ε_2, the absorption curve) of the dielectric permittivity as a function of photon energy for the $(C_6H_9N_2)_3[BiCl_6]$ compound. The real component, ε_1, provides insight into the reduction of the light velocity within the material, whereas the imaginary component, ε_2, reflects the absorption of incident light energy resulting from dipole motion. As illustrated in Fig. 13, both $\varepsilon_1(\lambda)$ and $\varepsilon_2(\lambda)$ display trends similar to those of the refractive index, which can be attributed to the relatively small values of the extinction coefficient K.

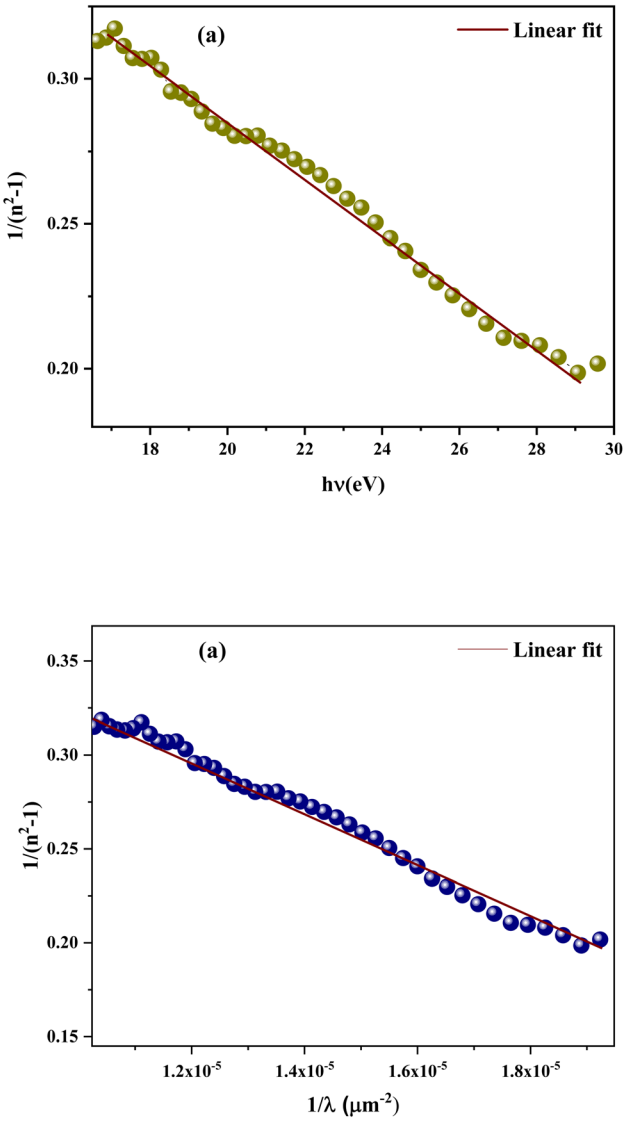

Fig. 12 Evolution of $1/(n^2\text{-}1)$ *versus*: (a) the photon energy and (b) $1/\lambda^2$, relative to the $(C_6H_9N_2)_3[BiCl_6]$ compound.

3.6 Complex impedance spectroscopy (CIS) studies (electrical properties)

To fully understand the electrical conduction behavior in the synthesized compound, we performed complex impedance measurements across a temperature range of 333–443 K. In this analysis, the real (Z') and imaginary (Z'') components of the complex impedance were examined separately to gain deeper insights into the material's electrical properties.[63–67]

The complex impedance (Z^*) is given by the following equation:

$$Z^* = Z' + jZ'' \quad (14)$$

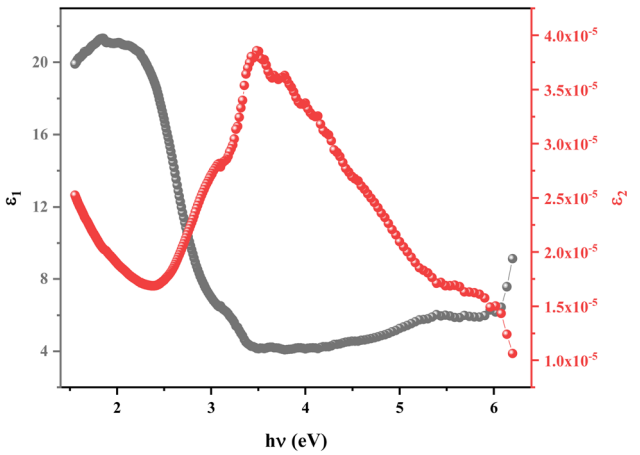

Fig. 13 Evolution of the real part ε_1 (a) and the imaginary part ε_2 of the dielectric permittivity *versus* photon energy for the $(C_6H_9N_2)_3[BiCl_6]$ compound.

3.6.1 Complex impedance measurements. Fig. 14 shows the Nyquist plots (Z'' *vs.* Z') for $(C_6H_9N_2)_3[BiCl_6]$ covering a temperature range from 333 K to 443 K. The impedance spectra exhibit a single, depressed semicircular arc across the entire temperature range. As the temperature rises, the semicircle radius decreases, indicating a reduction in sample resistance and an enhancement in conductivity.[68] The complex impedance spectra were analyzed using Z-View software, and the best fit was achieved with an equivalent circuit (illustrated in the inset of Fig. 14). This circuit comprises a parallel combination of resistance (R_1), capacitance (C_1), and a constant phase element (CPE_1) to account for the grain boundary effect. The excellent agreement between the experimental Nyquist data and the theoretical curve (solid line), derived from the estimated parameters, confirms the validity of the proposed circuit model.

The impedance of the CPE is expressed by:[69]

$$Z_{CPE} = \frac{1}{Q(j\omega)^{\alpha}} \quad (15)$$

here Q denotes the fractal capacitance, and α refers to the line's divergence from the vertical in the Nyquist plot. Table 2 shows the corresponding circuit characteristics.

The results show an exponential decrease in resistivity with increasing temperature, confirming the semiconductor nature of the sample and its negative temperature coefficient of resistance (NTCR) behavior.[70,71] Hybrid materials generally exhibit a decrease in grain boundary resistance as temperature rises because of the thermal activation of localized charge carriers, which increases their mobility and, as a result, increases hopping conduction and, in turn, decreases resistive behavior with temperature.[72]

The bulk conductivity σ_i at each temperature was derived by applying the formula:

$$\sigma_i = \frac{e}{S \times R_i} \quad (16)$$

where (e/s) denotes the geometrical ratio sample and R_i represents the resistance of the pellet deduced from Table 2.

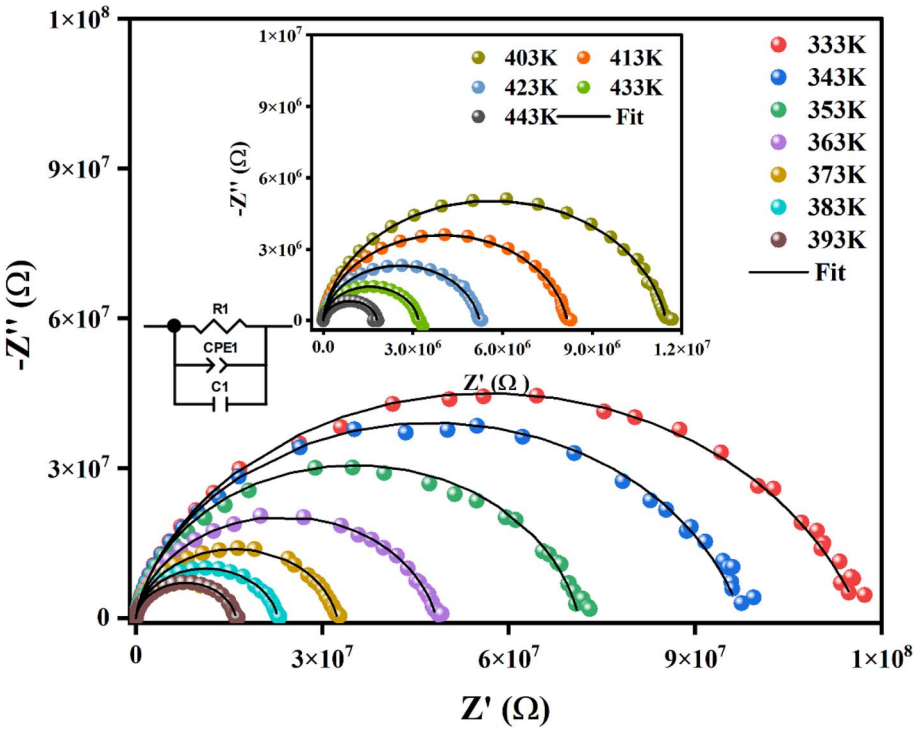

Fig. 14 Nyquist plots of $(C_6H_9N_2)_3[BiCl_6]$ at different temperatures. The inset represents the equivalent circuit, and the calculated responses based on this circuit are given by the fitted lines.

Table 2 Electrical fitted circuit parameters for $(C_6H_9N_2)_3[BiCl_6]$ at different temperatures

T (K)	R (10^6 Ω)	C (10^{-11} F)	Q (10^{-10} F)	α
443	1.794 836	3.026	1.0522	0.9707
433	3.16335	3.111	1.1961	0.97107
423	5.17428	3.113	0.840344	0.93805
413	8.03845	3.053	2.14476	0.98401
403	11.2909	2.341	0.91878	0.9451
393	15.8265	1.8751	0.734 124	0.89533
383	22.5668	4.09167	1.01595	0.81739
373	32.1464	2.76566	1.1657	0.86017
363	44.8858	5.06084	1.03958	0.78132
353	67.6201	6.89434	1.96215	0.55683
343	96.2001	5.33588	1.81857	0.70886
333	111.56	4.22289	1.53012	0.70603

These equations were used to compute the grain border conductivity:

$$\sigma_R = \frac{e}{S \times R_1} \quad (17)$$

Fig. 15 presents the variation of electrical conductivity at the grain boundary (σ_R) as a function of temperature. The observed conductivity behavior reveals a thermally activated transport mechanism that adheres to the Arrhenius equation:

$$\sigma_R = \sigma_0 \exp\left(\frac{-E_a}{k_B T}\right) \quad (18)$$

Where σ_0 refers to the pre-exponential factor and E_a is the conductivity's activation energy. The variation of the conductivity shows two regions, associated with two activation energies $E_{a1} = 0.42$ (0.007) eV, $\sigma_0 = 9.16\ 10^3$ (3.22) S cm^{-1} in the range [333–403 K] and $E_{a2} = 1.8$ (0.04) eV, $\sigma_0 = 2.73$ (1.22) S cm^{-1} in the range [403– 443 K]. The change in slope observed around 403 K confirms the phase transition identified through DSC measurements.

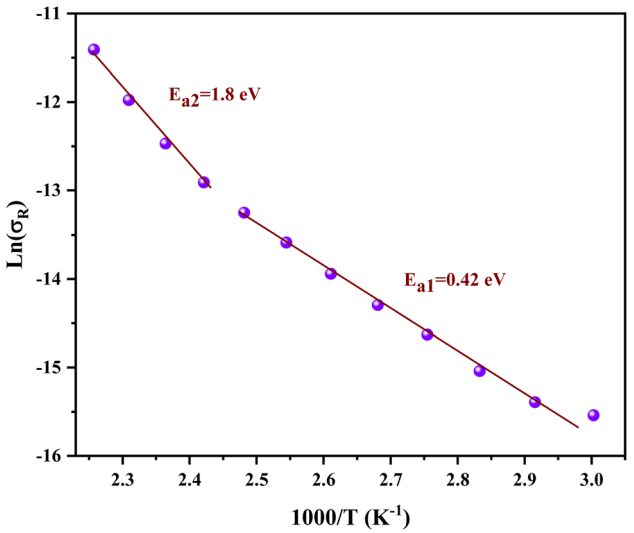

Fig. 15 Variation of ln(σ_R) as a function of temperature.

Using the proposed equivalent circuit, the real and imaginary components of the complex impedance formalism were quantitatively defined as follows:

$$Z' = \frac{R^{-1} + Q\omega^{\alpha}\cos\left(\frac{\alpha\pi}{2}\right)}{\left(R^{-1} + Q\omega^{\alpha}\cos\left(\frac{\alpha\pi}{2}\right)\right)^2 + \left(C\omega + Q\omega^{\alpha}\sin\left(\frac{\alpha\pi}{2}\right)\right)^2} \quad (19)$$

$$Z'' = \frac{C\omega + Q\omega^{\alpha}\sin\left(\frac{\alpha\pi}{2}\right)}{\left(R^{-1} + Q\omega^{\alpha}\cos\left(\frac{\alpha\pi}{2}\right)\right)^2 + \left(C\omega + Q\omega^{\alpha}\sin\left(\frac{\alpha\pi}{2}\right)\right)^2} \quad (20)$$

Fig. S3(a) illustrates the evolution of the real part of the complex impedance, $Z'(\omega)$, as a function of angular frequency over the temperature range of 333–443 K. Across all temperatures, Z' is higher at low frequencies and decreases progressively with increasing temperature, indicating enhanced charge transport dynamics. This indicates that the material is semiconductor-like and implies that $(C_6H_9N_2)_3[BiCl_6]$ possesses a negative temperature coefficient of resistance (NTCR). The decrease in barrier characteristics with increasing frequency and temperature indicates the release of space charge polarization,[58,59] resulting in a significant reduction in resistance to a nearly constant value at high frequencies. At these elevated frequencies, the available relaxation time becomes too short for space charge to fully respond, leading to an increased recombination rate and the subsequent release of trapped charges. This phenomenon is evidenced by the convergence of real impedance values at high frequencies across all temperatures.

Fig. S3(b) illustrates the evolution of (Z'') on angular frequency over the temperature range of 333–443 K. In this figure, Z'' gradually increases at low frequencies until it reaches a maximum value, Z''_{max}, at the material's characteristic relaxation frequency, or ω_{max}.[73,74] Beyond ω_{max}, Z'' decreases for all temperatures, eventually becoming constant at higher frequencies. This frequency-independent behavior of Z'' can be attributed to the dipoles' inability to respond to higher frequency AC signals, which reduces polarization. As temperature increases, the height of each peak decreases, and the peak positions shift towards higher frequencies. The peak height reflects the resistance of the process, so a decrease in peak height indicates a reduction in impedance, likely due to increased polaron mobility with higher temperatures.[75] This trend suggests shorter relaxation times with rising temperatures, demonstrating that the material exhibits space charge relaxation dependent on temperature.

The excellent agreement between the experimental data and the simulated curves, generated using eqn (7) and (8) and presented in Fig. S3(a) and (b), confirms the high accuracy of the extracted parameter values for the equivalent circuit.

Fig. S3(c) displays the scaling curve of the electric impedance for $(C_6H_9N_2)_3[BiCl_6]$. In this plot, each angular frequency is normalized by the relaxation frequency, ω_{max}, and $Z''(\omega)$ is normalized by its maximum value, Z''_{max}. The alignment of impedance spectra across different temperatures onto a single master curve suggests that the dynamic processes in the

$(C_6H_9N_2)_3[BiCl_6]$ sample remain unaffected by temperature variations.[76]

3.6.2 Conductivity analysis. In this section, we will explore the transport properties of the synthesized $(C_6H_9N_2)_3[BiCl_6]$ compound by examining its conductivity and applying a theoretical model. The model provides insights into the primary conduction processes that govern the transport properties. The literature includes several conduction models that describe charge carrier dynamics in hybrid organic–inorganic systems.[77–80] The total electrical conductivity contains of both direct current (DC) and alternating current (AC) components.[81,82] The DC component represents the steady-state conductivity observed at low frequencies, while the AC component reflects the frequency-dependent behavior seen at high frequencies. Fig. 16(a) illustrates the total conductivity (σ) *versus* angular frequency over the studied temperatures range. Each conductivity spectrum in this study is analyzed using the simple Jonscher law:[83]

$$\sigma(\omega,T) = \sigma_{DC}(T) + B(T)\omega^{s(T)} \quad (21)$$

The first term characterizes the variation in DC electrical conductivity in the studied compound. The second term is introduced to examine the prepared compound's electrical behavior in the spectra's dynamic region, specifically focusing on AC electrical conductivity. The frequency exponent (s) characterizes the extent of interaction between mobile charge carriers and offers valuable insight into the underlying mechanisms of electrical conduction. Table 3 displays the obtained fitting parameters.

Fig. 16(b) depicts the variation of $\ln(\sigma_{dc})$ *versus* $(1000/T)$, highlighting two distinct linear regions. This behavior indicates an increase in conductivity with increasing temperature, further confirming the semiconductor properties of the studied compound. Across the investigated temperature range, the data adhere to the Arrhenius relation, a widely recognized model for describing the temperature dependence of electrical conductivity in organic–inorganic hybrid materials:[84]

$$\sigma_{dc} = \sigma_0 \exp\left(\frac{-E_a}{k_B T}\right) \quad (22)$$

The parameter σ_0 is the electrical conductivity (pre-exponential factor); the parameter k_B represents Boltzmann's constant, and E_a is the activation energy. The electrical transport of charge carriers above 403 K is represented by an activation energy value of E_a = 0.79 (0.03) eV, σ_0 = 96.1 (2.93) S cm^{-1}. In contrast, the activation energy within the lower temperature range (333–403 K) is 0.42 (±0.008) eV, with a pre-exponential factor of σ_0 = 304 (±1.35) S cm^{-1}. These values are similar to those determined by the σ_R conductivity.

In the AC regime, the conduction process is characterized by plotting the temperature dependence of the frequency exponent "s" (Fig. 16(c)). As illustrated in Fig. 16(c), at lower temperatures, the frequency exponent approaches unity for the sample under investigation. This trend suggests that the transport properties

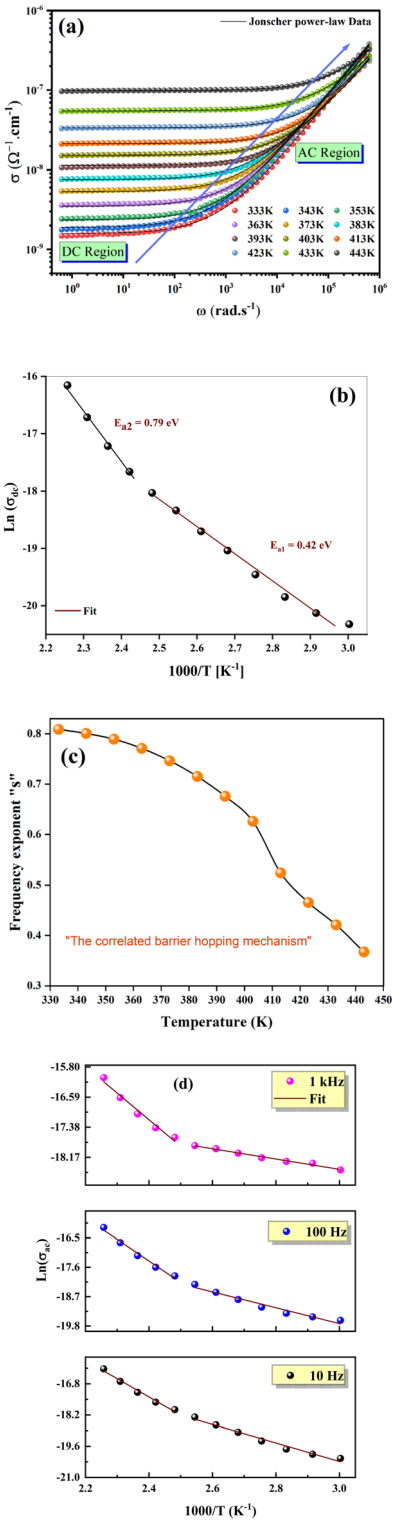

Fig. 16 (a) Variation of the ac electrical conductivity *vs.* the frequency at different temperatures, (b) variation of direct current conductivity as a function of temperature, (c) variation of the parameter s as a function of temperature and (d) temperature dependence of the AC conductivity at different frequencies.

are governed by the hopping of charge carriers between oppositely charged states, overcoming a potential barrier.[85] For conduction to occur, charge carriers must overcome this

Table 3 The list of parameters obtained by fitting the Jonscher law function to the frequency-dependent electrical conductivity data

T (K)	σ_{DC} ($\times 10^{-9}$ S cm^{-1})	s
333	1.491	0.808
343	1.814	0.800
353	2.399	0.789
363	3.549	0.770
373	5.399	0.746
383	7.552	0.715
393	0.108	0.675
403	0.147	0.625
413	0.212	0.524
423	0.332	0.465
433	0.550	0.420
443	0.962	0.367

potential barrier. Consequently, the observed $s(T)$ behavior points to a correlated barrier hopping (CBH) conduction mechanism.[79]

The correlated barrier hopping (CBH) model was first refined by Pike to explain single-polaron hopping and later extended by Elliott to incorporate two-polaron hopping mechanisms. In this framework, the charge carriers move between localized states separated by a potential barrier. According to the CBH model, the parameter s can be expressed by the following relation:

$$s(T) = 1 - \frac{6k_B T}{W_M + k_B T \ \ln(\omega\tau_0)} \quad (23)$$

where, T is the absolute temperature, k_B is Boltzmann's constant, W_m denotes the binding energy corresponding to the complete transfer of an electron between two sites, and τ_0 represents the characteristic relaxation time of the carriers. At low temperatures ($k_B T \ln(1/\omega\tau_0) << W_M$), this relation can be simplified, and the expression for s takes the form:

$$s(T) = 1 - \frac{6k_B T}{W_M} \quad (24)$$

Furthermore, the density of states at the Fermi level, $N(E_F)$, was evaluated using AC conductivity data through the relation.[86]:

$$\sigma_{ac} = n\frac{\pi^2}{24} N N_p \varepsilon' \omega R_\omega{}^6 \quad (25)$$

Fig. 16(d) shows the variation of $\ln(\sigma_{ac})$ with $(1000/T)$ for the studied compound. The experimental data (symbols) are in excellent agreement with the theoretical fitting (solid lines), confirming that the CBH model is the most reliable framework to describe the frequency-dependent AC conductivity across both low- and high-frequency regions. The parameters obtained from the fitting process are summarized in Table S5. The data show that as frequency increases, U_{eff} decreases, which supports the idea of ionic conduction through hopping in this range of temperatures and frequencies.[87–89] In addition, the rise in N_T with increasing frequency explains the corresponding growth in AC conductivity.

3.6.3 Electric modulus. The modulus framework is used to study the transport behavior and relaxation phenomena in organic–inorganic systems, which are characterized by the accumulation and movement of charge carriers.[90] According to previous investigations,[91,92] space charge polarization can lead to partial dielectric breakdown or discharge and electrode polarization, which significantly increases permittivity and complicates the analysis of organic–inorganic compounds. In this context, the complex electric modulus serves as a crucial tool for understanding the electrical and dielectric properties of materials. Extensive research demonstrates that the electric modulus effectively clarifies the underlying mechanisms of dielectric relaxation.

Fig. 17(a) shows the temperature-dependent M'' as a function of angular frequency for the $(C_6H_9N_2)_3[BiCl_6]$ compound. The M'' spectra exhibit well-defined peaks at characteristic angular frequencies (ω_p). For each temperature, the presence of

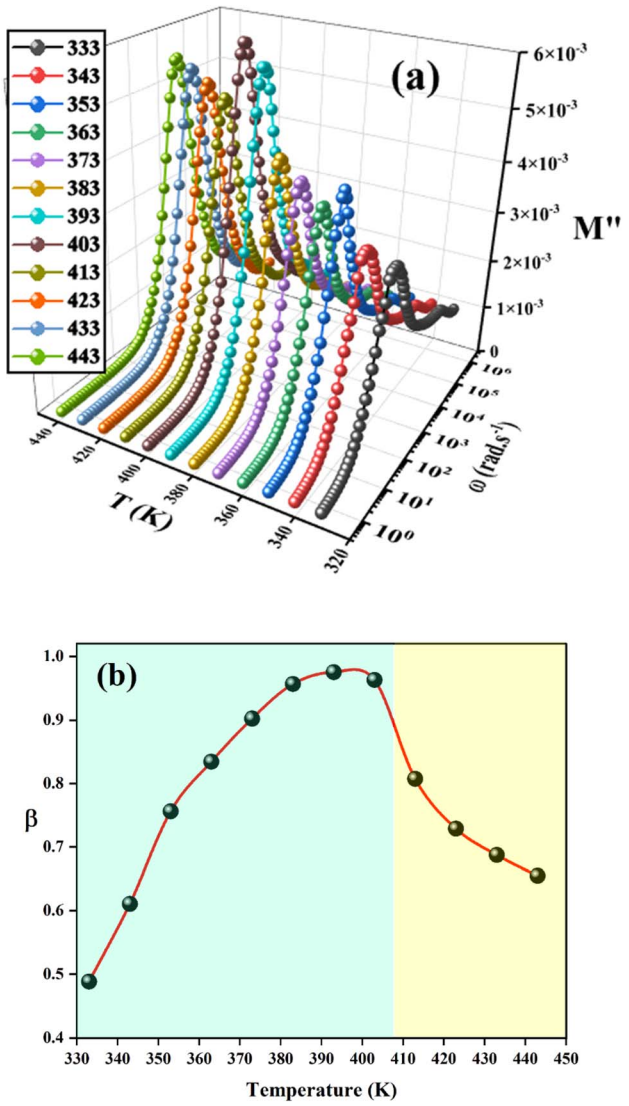

Fig. 17 Frequency dependence of M″ at different temperatures of $(C_6H_9N_2)_3[BiCl_6]$, and (b) variation of β parameter with temperature.

a relaxation peak at a specific frequency indicates a transition from short-range to long-range mobility behaviors.[93] At high frequencies, the charge carriers responsible for the material's electrical and dielectric properties become trapped in localized states. Below (ω_p), the conduction properties of $(C_6H_9N_2)_3[BiCl_6]$ are associated with long-range hopping of charges.[94] Additionally, short-range hopping of charge carriers and its dynamics are evident above the relaxation frequency. At higher temperatures, the asymmetric behavior observed in the M'' spectra, along with the shifts of the M'' peak positions toward higher frequencies, is associated with the increasing degree of relaxation due to the activation of charge carriers. Furthermore, this result suggests the presence of non-Debye relaxation in $(C_6H_9N_2)_3[BiCl_6]$. To further explore the nature of dielectric relaxation in the material based on the frequency dependence of M'', we propose using the following expression to determine the β parameter:[94]

$$M''(\omega) = \frac{M''_p(\omega)}{\left[1-\beta+\left(\frac{\beta}{\beta+1}\right)\left[\beta\left(\frac{\omega_p}{\omega}\right)+\left(\frac{\omega}{\omega_p}\right)^{\beta}\right]\right]} \quad (26)$$

$M''_P(\omega)$ represents the peak maximum of M'', while ω_p indicates the peak frequency. The exponent β offers insight into the nature of the relaxation in the material. In an ideal dielectric compound, β equals 1, signifying minimal dipole–dipole interaction (Debye relaxation). When β is less than 1, it indicates significant dipole–dipole interactions (non-Debye relaxation).[68]

For the $(C_6H_9N_2)_3[BiCl_6]$ material under study, the results shown in Fig. 17(b) indicate that β is less than 1. This observation confirms the occurrence of non-Debye relaxation in the sample's conductivity. The variation in the β parameter reveals two distinct regions, with a noticeable change in slope around 413 K. This observation confirms the changes in electrical properties, validating the thermal behavior and phase transition.

3.7 Dielectric properties

Upon initial consideration, increasing the dielectric constant may appear to be the optimal strategy for achieving competitive quality in electric energy storage. To pursue this effectively, it is essential to understand the polarization mechanisms influencing the dielectric properties of materials. Polarization processes are well-known to be the primary contributors to a material's specific dielectric characteristics. The most common polarization mechanisms include interfacial, ionic, dipolar, atomic, and electronic types. Here, the focus is on interfacial polarization, a key phenomenon for investigating electrical conductivity.

Interfacial, or space-charge, polarization arises from the accumulation of charge carriers at interfaces in response to an external electric field. This can occur at the interfaces between different materials or within different regions of the same material, such as at electrode-insulator contact surfaces, interface borders, and grain boundaries. Interfacial polarization impacts not only the covalent and bonded structures of dielectric materials but also involves the accumulation of free charges.[95–100]

Space-charge polarization is distinct from electronic, atomic, and ionic polarization in terms of its relaxation frequency range. Its relaxation frequency appears at low frequencies, below 10^6 Hz (the range used in these experiments), while electronic polarization occurs around 10^{15} Hz, atomic polarization from 10^{12} to 10^{13} Hz, and orientation polarization between 10^9 and 10^{11} Hz.

Fig. S4 displays the frequency dependence of the real part (ε') for $(C_6H_9N_2)_3[BiCl_6]$ at different temperatures. At approximately 25 °C and 1 MHz, the real permittivity (ε') reaches a value of 80, which is comparable to that observed in the compound $(C_6H_9N_2)_2[SbBr_4]Br$.[36] The elevated permittivity observed at low frequencies is attributed to enhanced charge accumulation at interfaces, as longer time intervals enable dipoles to align fully with the applied electric field. As the frequency increases, ε' gradually decreases due to the Maxwell-Wagner,[101,102] interfacial polarization effect, which arises because charges cannot follow the rapidly oscillating electric field at higher frequencies. This behavior manifests as a high dielectric constant at low frequencies and a decline at higher frequencies due to the inability of dipoles to reorient quickly.

Beyond the direct observation of permittivity, the dielectric response of $(C_6H_9N_2)_3[BiCl_6]$ is consistent with the presence of space-charge polarization mechanisms, which are critical for explaining its significant dielectric constant and frequency-dependent behavior. When combined with related $BiCl_6$-based compounds reported in the literature,[31,103–105] these results confirm the intrinsic capability of this class of organic–inorganic hybrids to exhibit substantial dielectric responses arising from the interactions of the organic cations with the inorganic bismuth chloride octahedra.

To further investigate temperature-dependent dipolar polarization and associated relaxation phenomena, the dielectric data were analyzed using the Cole–Davison model, represented by the following equation:[98,106]

$$\varepsilon = \varepsilon_\infty + \frac{\varepsilon_s - \varepsilon_\infty}{1+(i\omega\tau)^\beta} \quad (27)$$

The real and imaginary components of permittivity are given by:

$$\varepsilon' = \varepsilon_\infty + \frac{(\varepsilon_s-\varepsilon_\infty)\cos[\beta\arctan(\omega\tau)}{\left[1+(\omega\tau)^2\right]^{\frac{\beta}{2}}} \quad (28)$$

$$\varepsilon'' = \frac{(\varepsilon_s-\varepsilon_\infty)\sin[\beta\arctan(\omega\tau)}{\left[1+(\omega\tau)^2\right]^{\frac{\beta}{2}}} \quad (29)$$

were ω represents the angular frequency, τ denotes the relaxation time, and β is a material-specific constant associated with the broadening of the relaxation time distribution. The parameters ε_s and ε_∞ correspond to the static (low-frequency) and high-frequency dielectric constants, respectively.

Eqn (28) was employed to fit the experimental real part of the dielectric constant as a function of frequency (Fig. S4) to extract key dielectric and relaxation properties of the $(C_6H_9N_2)_3[BiCl_6]$ sample. The parameters obtained from these fits are summarized in Table S6.

In comparison with other recently reported lead-free halide hybrids,[20,107–110] the phase transition temperature of $(C_6H_9N_2)_3[BiCl_6]$, observed at 420 K, highlights its superior thermal stability. While many analogous compounds display transitions in the lower 300–400 K range, the higher transition temperature recorded here suggests enhanced structural robustness, which is advantageous for device operation under elevated temperatures. This intrinsic thermal resilience, coupled with the compound's significant dielectric constant and notable electrical conductivity, underscores its potential as a high-performing material for energy storage and optoelectronic technologies. By elucidating the dielectric mechanisms governing its response, our study contributes to the advancement of environmentally friendly hybrid halides designed for next-generation capacitors and other electronic applications.

4 Conclusion

In conclusion, the hybrid compound $(C_6H_9N_2)_3[BiCl_6]$ exhibits a promising combination of structural, thermal, optical, electrical, and dielectric properties, positioning it as a strong candidate for advanced technological applications. The successful synthesis *via* the slow evaporation method resulted in a triclinic structure within the $P\bar{1}$ space group, with a notable phase transition occurring at 420 K. Optical characterization through UV-visible absorption spectroscopy underscores its semiconducting potential. Electrical and dielectric analyses revealed a non-Debye relaxation process, a strong dependence on frequency and temperature, and conduction governed by the correlated barrier-hopping (CBH) model. Furthermore, its high dielectric constant at low frequencies highlights its significant potential for energy storage applications.

Overall, this study not only provides fundamental insights into the multifunctional capabilities of $(C_6H_9N_2)_3[BiCl_6]$ but also emphasizes its relevance in semiconductor technology and energy storage systems. By exploring the intricate properties of organic–inorganic hybrid materials, our research contributes to the ongoing development of cost-effective, high-performance alternatives to conventional semiconductors and energy storage solutions, paving the way for future innovations in these fields.

Author contributions

Rima Altalib: writing – original draft, validation, software, methodology, investigation. Arafet Ghoudi: writing – original draft, validation, software, methodology, investigation. Mohamed Tliha: writing – original draft, visualization, formal analysis. Raja Naouari: writing review & editing, writing – original draft, validation, methodology. Walid Rekik: writing review & editing, validation, methodology. Jerome Lhoste: writing review & editing, investigation, methodology Abderrazek Oueslati. writing – review & editing, visualization, validation, investigation, formal analysis, data curation.

Conflicts of interest

The authors declare that they have no known financial conflicts of interest or personal relationships that could have influenced the research presented in this paper.

Data availability

CCDC 2366479 contains the supplementary crystallographic data for this paper.[111]

The datasets used and/or analyzed during the current study are available from the corresponding author upon reasonable request. Supplementary information is available. See DOI: https://doi.org/10.1039/d5ra01766a.

Acknowledgements

The authors extend their appreciation to Umm Al-Qura University, Saudi Arabia for funding this research work through grant number: 25UQU4331138GSSR07.

References

1 H. Elgahami, W. Trigui, A. Oueslati and F. Hlel, *Ionics*, 2019, **25**, 1359–1371.
2 S. Hermi, M. G. Althobaiti, A. A. Alotaibi, A. H. Almarri, W. Fujita, F. Lefebvre, C. Ben Nasr and M. H. Mrad, *Crystals*, 2021, **11**, 553.
3 L. Zhang, J. Wang, J. Wu, S. Mo, F. Long, Z. Zou and Y. Gao, *J. Mater. Sci.: Mater. Electron.*, 2018, **29**, 9821–9828.
4 S. Jarboui, C. Hrizi, A. Oueslati and F. Zouari, *Inorg. Chim. Acta*, 2024, **561**, 121876.
5 S. Bougossa, N. Mhadhbi, A. B. Ahmed, M. Hamdi, K. Elghniji, J. Erwann, K. Hamden, A. Oueslati and H. Naïli, *RSC Adv.*, 2024, **14**, 17413–17433.
6 X. Lu, L. Zhang, Y. Tong and Z. Y. Cheng, *Composites, Part B*, 2019, **168**, 34–43.
7 Y. Wang, T. Guo, J. Yin, Z. Tian, Y. Ma, Z. Liu, Y. Zhu and H. N. Alshareef, *Adv. Mater.*, 2022, **34**, 2106937.
8 L. T. López, D. Ramírez, F. Jaramillo and J. A. Calderón, *Electrochim. Acta*, 2020, **357**, 136882.
9 D. Yang, L. Luo, Y. Gao, S. Chen and X. C. Zeng, *Mater. Horiz.*, 2019, **6**, 1463–1473.
10 M. Rok, B. Zarychta, J. Trojan-Piegza, A. Bil, A. Piecha-Bisiorek, J. K. Zaręba, W. Medycki and R. Jakubas, *J. Mater. Chem. C*, 2022, **10**, 3036–3047.
11 X. Liu, W. Xu, S. Xu, X. Yu, Y. Deng, X. Wu, F. Liang and Q. Wu, *Inorg. Chem.*, 2020, **59**, 5721–5727.
12 D. Lencer, M. Salinga and M. Wuttig, *Adv. Mater.*, 2011, **23**, 2030–2058.
13 P.-F. Li, W.-Q. Liao, Y.-Y. Tang, H.-Y. Ye, Y. Zhang and R.-G. Xiong, *J. Am. Chem. Soc.*, 2017, **139**, 8752–8757.
14 S. Gatfaoui, A. Sagaama, N. Issaoui, T. Roisnel and H. Marouani, *Solid State Sci.*, 2020, **106**, 106326.

15 H. Elgahami, A. Oueslati, S. Nasr, F. Costantino and H. Naïli, *RSC Adv.*, 2023, **13**, 26122–26133.
16 A. Jellali, N. Karâa, H. Ghalla and B. Hamdi, *Chem. Afr.*, 2024, **7**, 1649–1665.
17 H. Khachroum, M. Krimi, M. S. M. Abdelbaky, S. García-Granda and M. Dammak, *Mater. Res. Bull.*, 2024, **179**, 112978.
18 A. Mhiri, F. Krichen, A. Oueslati, J. Lhoste, F. Goutenoire, M. Gargouri and A. Bulou, *J. Alloys Compd.*, 2019, **772**, 546–556.
19 Y.-T. Liu, L. He, P.-P. Shi, Q. Ye and D.-W. Fu, *Chem. Commun.*, 2020, **56**, 13764–13767.
20 B. Kulicka, V. Kinzhybalo, R. Jakubas, Z. Ciunik, J. Baran and W. Medycki, *J. Phys.: Condens. Matter*, 2006, **18**, 5087.
21 M.-Q. Li, Y.-Q. Hu, L.-Y. Bi, H.-L. Zhang, Y. Wang and Y.-Z. Zheng, *Chem. Mater.*, 2017, **29**, 5463–5467.
22 A. M. Goforth, M. D. Smith, P. LeRoy and H.-C. zur Loye, *Inorg. Chem.*, 2004, **43**, 7042–7049.
23 J. Tarasiewicz, R. Jakubas, J. Baran and A. Pietraszko, *J. Mol. Struct.*, 2006, **792–793**, 265–273.
24 C. H. R. Krishna, U. S. U. Thampy, D. v. Sathish, C. H. V. Reddy, A. v. Chandrasekhar, Y. p. Reddy, P. s. Rao and R. V. S. S. N. Ravikumar, *J. Coord. Chem.*, 2011, **64**, 4276–4285.
25 S. Hermi, A. A. Alotaibi, F. Lefebvre, C. Ben Nasr and M. H. Mrad, *J. Mol. Struct.*, 2020, **1216**, 128296.
26 A. Rayes, C. B. Nasr and M. Rzaigui, *Mater. Res. Bull.*, 2004, **39**, 571–580.
27 *Bruker APEX2, SADABS, SAINT-Plus and XPREP*, Bruker AXS Inc., Madison, Wisconsin, USA, 2009.
28 G. M. Sheldrick, *Acta Crystallogr., Sect. C:Struct. Chem.*, 2015, **71**, 3–8.
29 L. J. Farrugia, *J. Appl. Crystallogr.*, 1999, **32**, 837–838.
30 I. Chaabane, W. Rekik, H. Ghalla, M. Zaghrioui, J. Lhoste and A. Oueslati, *RSC Adv.*, 2024, **14**, 3588–3598.
31 H. Felhi, K. Mencel, A. Piecha-Bisiorek, R. Jakubas, V. Kinzhybalo and W. Medycki, *J. Mol. Struct.*, 2019, **1179**, 297–303.
32 A. S. Rao, U. Baruah and S. K. Das, *Inorg. Chim. Acta*, 2011, **372**, 206–212.
33 K. Kahouli, R. Mesbeh, M. S. M. Abdelbaky, S. García-Granda, A. Koumina and S. Chaabouni, *J. Mol. Struct.*, 2021, **1231**, 129826.
34 Z. Aloui, C. Ounelli, M. Essid, F. Nicolò, G. Bella, A. Santoro, S. Abid and G. Bruno, *J. Solid State Chem.*, 2022, **316**, 123572.
35 W. H. Baur, *Acta Crystallographica, Sect. B: Struct. Sci.Acta Crystallographica, Sect. B: Struct. Sci.*, 1974, **30**, 1195–1215.
36 I. Chaabane, W. Rekik, M. Zaghrioui, J. Lhoste, A. Oueslati and M. Gargouri, *Ionics*, 2024, **30**, 5827–5844.
37 C. Janiak, *J. Chem. Soc., Dalton Trans.*, 2000, 3885–3896.
38 N. J. Singh, S. K. Min, D. Y. Kim and K. S. Kim, *J. Chem. Theory Comput.*, 2009, **5**, 515–529.
39 H. Ferjani, H. Chebbi and M. Fettouhi, *Int. J. Mol. Sci.*, 2021, **22**, 2030.
40 A. Chtioui and A. Jouini, *J. Chem. Crystallogr.*, 2004, **34**, 43–49.
41 A. Chtioui, L. Benhamada and A. Jouini, *Mater. Res. Bull.*, 2005, **40**, 2243–2255.
42 J. H. Joshi, S. Kalainathan, M. J. Joshi and K. D. Parikh, *Arabian J. Chem.*, 2020, **13**, 5018–5026.
43 S. Dgachi, F. Rahmouni, A. Soran, M. Saoudi, G. Nemes and H. Naïli, *J. Mol. Struct.*, 2021, **1244**, 130996.
44 R. Elwej, N. Hannachi, I. Chaabane, A. Oueslati and F. Hlel, *Inorg. Chim. Acta*, 2013, **406**, 10–19.
45 M. Li, G.-C. Xu, Y.-Q. Zhang and W.-B. Xin, *J. Solid State Chem.*, 2020, **287**, 121329.
46 K. Ben Brahim, M. Ben Gzaiel, A. Oueslati, K. Khirouni, M. Gargouri, G. Corbel and J.-F. Bardeau, *RSC Adv.*, 2021, **11**, 18651–18660.
47 A. B. J. Kharrat, K. Kahouli and S. Chaabouni, *Bull. Mater. Sci.*, 2020, **43**, 275.
48 K. Kahouli, A. B. J. Kharrat and S. Chaabouni, *Indian J. Phys.*, 2021, **95**, 2797–2805.
49 A. Ghoudi, I. Chaabane, R. Naouari, A. Aydi, A. Oueslati, E. Dhahri, B. F. O. Costa, T. Nikitin, J. A. Paixão and R. Fausto, *Inorg. Chem. Commun.*, 2024, **168**, 112925.
50 R. Kalthoum, M. Ben Bechir and A. Ben Rhaiem, *Phys. E*, 2020, **124**, 114235.
51 J. H. Joshi, S. Kalainathan, D. K. Kanchan, M. J. Joshi and K. D. Parikh, *Arabian J. Chem.*, 2020, **13**, 1532–1550.
52 R. E. Marotti, D. N. Guerra, C. Bello, G. Machado and E. A. Dalchiele, *Sol. Energy Mater. Sol. Cells*, 2004, **82**, 85–103.
53 R. Henríquez, P. Grez, E. Muñoz, H. Gómez, J. A. Badán, R. E. Marotti and E. A. Dalchiele, *Thin Solid Films*, 2010, **518**, 1774–1778.
54 B. E. Sernelius, K.-F. Berggren, Z.-C. Jin, I. Hamberg and C. G. Granqvist, *Phys. Rev. B: Condens. Matter Mater. Phys.*, 1988, **37**, 10244–10248.
55 S. Gagandeep, K. Singh, B. S. Lark and H. S. Sahota, *Nucl. Sci. Eng.*, 2000, **134**, 208–217.
56 K. Souifi, O. Rejaiba, O. Amorri, M. Nasri, B. Alzahrani, M. L. Bouazizi, K. Khirouni and J. Khelifi, *J. Inorg. Organomet. Polym.*, 2022, **32**, 4515–4531.
57 Z. Yang, K. P. Homewood, M. S. Finney, M. A. Harry and K. J. Reeson, *J. Appl. Phys.*, 1995, **78**, 1958–1963.
58 S. Husain, A. O. A. Keelani and W. Khan, *Nano-Struct. Nano-Objects*, 2018, **15**, 17–27.
59 O. Rejaiba, K. Khirouni, M. H. Dhaou, B. Alzahrani, M. L. Bouazizi and J. Khelifi, *Opt. Quantum Electron.*, 2022, **54**, 315.
60 S. H. Wemple and M. DiDomenico, *Phys. Rev. B*, 1971, **3**, 1338–1351.
61 R. Lefi, F. Ben Naser and H. Guermazi, *J. Alloys Compd.*, 2017, **696**, 1244–1254.
62 M. A. Majeed Khan, M. Wasi Khan, M. Alhoshan, M. S. AlSalhi and A. S. Aldwayyan, *Appl. Phys. A*, 2010, **100**, 45–51.
63 J. H. Joshi, D. K. Kanchan, M. J. Joshi, H. O. Jethva and K. D. Parikh, *Mater. Res. Bull.*, 2017, **93**, 63–73.
64 S. Karoui and S. Kamoun, *Indian J. Phys.*, 2024, **98**, 2731–2744.

65 M. A. L. Nobre and S. Lanfredi, *Mater. Lett.*, 2001, **50**, 322–327.
66 J. H. Joshi, G. M. Joshi, M. J. Joshi and K. D. Parikh, *Ionics*, 2019, **25**, 3223–3245.
67 J. H. Joshi, D. K. Kanchan, H. O. Jethva, M. J. Joshi and K. D. Parikh, *Ionics*, 2018, **24**, 1995–2016.
68 S. Chkoundali, I. Garoui, W. Trigui and A. Oueslati, *RSC Adv.*, 2024, **14**, 8971–8980.
69 P. Córdoba-Torres, T. J. Mesquita, O. Devos, B. Tribollet, V. Roche and R. P. Nogueira, *Electrochim. Acta*, 2012, **72**, 172–178.
70 Y. Moualhi, H. Rahmouni and F. Bahri, *Sens. Actuators, A*, 2024, **377**, 115596.
71 Y. Mateyshina, A. Slobodyuk, V. Kavun and N. Uvarov, *Solid State Ionics*, 2018, **324**, 196–201.
72 A. Ghoudi, S. Auguste, J. Lhoste, W. Rekik, H. Ghalla, K. Khirouni, A. Aydi and A. Oueslati, *ACS Omega*, 2024, **9**, 28339–28353.
73 D. K. Mahato and T. P. Sinha, *J. Alloys Compd.*, 2015, **634**, 246–252.
74 L. H. Omari, R. Moubah, A. Boutahar, L. Hajji and R. El Ouatib, *J. Electroceram.*, 2020, **44**, 23–31.
75 N. Moutia, A. Oueslati, M. Ben Gzaiel and K. Khirouni, *Phys. E*, 2016, **83**, 88–94.
76 A. Sahoo, T. Paul, P. Pal, N. H. Makani, A. Ghosh and R. Banerjee, *Phys. Rev. Appl.*, 2023, **20**, 034024.
77 A. Ghosh and D. Chakravorty, *J. Phys.: Condens. Matter*, 1990, **2**, 5365.
78 X. L. Cleac'h, *J. Phys.*, 1979, **40**, 417–428.
79 G. E. Pike, *Phys. Rev. B*, 1972, **6**, 1572–1580.
80 S. R. Elliott, *Philos. Mag. B*, 1978, **37**, 553–560.
81 S. Karoui, H. Chouaib and S. Kamoun, *J. Solid State Chem.*, 2017, **254**, 109–118.
82 J. H. Joshi, G. M. Joshi, M. J. Joshi, H. O. Jethva and K. D. Parikh, *New J. Chem.*, 2018, **42**, 17227–17249.
83 A. K. Jonscher, *Nature*, 1977, **267**, 673–679.
84 M. ben gzaiel, I. Garoui, F. N. Almutairi, I. Mbarek and O. A, *Opt. Mater.*, 2024, **154**, 115664.
85 Y. Moualhi, M. Smari and H. Rahmouni, *RSC Adv.*, 2023, **13**, 30010–30021.
86 A. Zaafouri, M. B. Gzaiel, I. Gharbi, B. Bakri and A. Oueslati, *J. Mater. Sci.: Mater. Electron.*, 2024, **35**, 814.
87 G. Singh, N. Goyal, G. S. S. Saini and S. K. Tripathi, *J. Non-Cryst. Solids*, 2007, **353**, 1322–1325.
88 W. R. Buessem and M. Kahn, *J. Am. Ceram. Soc.*, 1971, **54**, 458–461.
89 A. K. Jonscher, *Thin Solid Films*, 1983, **100**, 329–334.
90 K. Kahouli, A. kahouli, K. Khirouni and S. Chaabouni, *J. Mol. Struct.*, 2020, **1199**, 126944.
91 S. Karoui, H. Chouaib and S. Kamoun, *J. Phys. Org. Chem.*, 2020, **33**, e4101.
92 Y. Moualhi, M. Smari, H. Nasri and H. Rahmouni, *Mater. Today Commun.*, 2024, **38**, 108529.
93 S. B. Yahya and B. Louati, *J. Alloys Compd.*, 2021, **876**, 159972.
94 S. B. Yahya, R. Barillé and B. Louati, *RSC Adv.*, 2022, **12**, 6602–6614.
95 J. H. Joshi, K. V. Vadhel, G. M. Joshi, M. J. Joshi, H. O. Jethva and K. D. Parikh, *Chin. J. Phys.*, 2020, **65**, 268–291.
96 L. Zhu and Q. Wang, *Macromolecules*, 2012, **45**, 2937–2954.
97 A. R. Blythe and D. Bloor, *Electrical Properties of Polymers*, Cambridge University Press, 2005.
98 F. Kremer and A. Schönhals, *Broadband Dielectric Spectroscopy*, Springer Science & Business Media, 2002.
99 R. Thakur, D. Das and A. Das, *Sep. Purif. Rev.*, 2013, **42**, 87–129.
100 J. H. Joshi, K. V. Vadhel, G. M. Joshi, S. Kalainathan, M. J. Joshi, H. O. Jethva and K. D. Parikh, *Chin. J. Phys.*, 2020, **64**, 138–162.
101 Z.-M. Dang, J.-K. Yuan, S.-H. Yao and R.-J. Liao, *Adv. Mater.*, 2013, **25**, 6334–6365.
102 J. H. Joshi, S. A. M. B. Dhas, D. K. Kanchan, M. J. Joshi and K. D. Parikh, *J. Mater. Sci.: Mater. Electron.*, 2020, **31**, 14859–14878.
103 N. Elfaleh and S. Kamoun, *Ionics*, 2015, **21**, 2685–2692.
104 K. Kahouli, A. B. J. Kharrat, K. Khirouni and S. Chaabouni, *Appl. Phys. A*, 2023, **129**, 431.
105 W. Masmoudi, S. Kamoun and M. Gargouri, *Ionics*, 2012, **18**, 117–126.
106 D. W. Davidson and R. H. Cole, *J. Chem. Phys.*, 1951, **19**, 1484–1490.
107 H. Peng, Q. Liu, Y. Liu, Y. Lu and W. Liao, *Chin. Chem. Lett.*, 2023, **34**, 107980.
108 J. Jóźków, W. Medycki, J. Zaleski, R. Jakubas, G. Bator and Z. Ciunik, *Phys. Chem. Chem. Phys.*, 2001, **3**, 3222–3228.
109 A. Ouasri, H. Jeghnou, A. Rhandour and P. Roussel, *J. Solid State Chem.*, 2013, **200**, 22–29.
110 A. Ouasri, *Rev. Inorg. Chem.*, 2023, **43**, 247–280.
111 R. Altalib, A. Ghoudi, M. Tliha, R. Naouari, W. Rekik, J. Lhoste and A. Oueslati, CCDC 2366479: Experimental Crystal Structure Determination, 2025, DOI: **10.5517/ccdc.csd.cc2kfj1l**.